PHYSICAL REVIEW B VOLUME 46, NUMBER 8 15 AUGUST 1992-II

Time-resolved patterns for electron-stimulated desorption of metastable atoms from thin Ar(111) films

G. Leclerc, A. D. Bass, A. Mann, and L. Sanche
Groupe du Conseil de Recherches Médicales en Sciences des Radiations, Faculté de Médecine, Université de Sherbrooke, Sherbrooke, Québec, Canada J1H 5N4

(Received 21 January 1992)

Time-resolved desorption patterns of metastable argon atoms have been obtained from thin Ar(111) films condensed on Pt(111) at 15 K. The desorption is stimulated by monochromatic electrons with a fixed energy of 14.5 eV. Combining the information on time-of-flight and angular distributions, five distinct metastable-atom components can be identified. The maxima of their kinetic energies are located at 19, 36, 53, 85, and 345 meV (±10%), with the two lowest-energy signals being more intense. The 53-meV component has a narrow angular distribution of 8° at half maximum with respect to the surface normal, while the others are broad. Different aspects of the basic desorption mechanisms are discussed. The sharpness of the angular distribution of the 53-meV component is interpreted as due to nuclear zero-point motion in an undistorted crystalline environment. The data for the 19-, 36-, and 53-meV components are in qualitative agreement with recent molecular-dynamics studies.

I. INTRODUCTION

The fundamental role of electronic excitation in the sputtering of rare-gas solids has been studied by several different experimental techniques over the past decade. On Ar, such studies have been performed with high-energy beams of electrons[1] or ions[2] to produce the excitation of the media. Photon-stimulated desorption (PSD) studies[3,4] have allowed the selective production of excited species at the surface or within the bulk. Luminescence measurements permit one to track the decay of the excited species within a film or after emission of an excited particle into vacuum,[4,5] while neutral atoms are often detected in time-of-flight (TOF) experiments.[1,6] Thus a detailed view of the desorption of neutral ground-state atoms has been achieved for the rare-gas solids.

Only recently, a gap in the data has been closed with reports on metastable-atom desorption after electron or photon impact. In a previous publication on desorption of metastable Ar atoms,[7] we presented high-resolution excitation functions for electron energies between 10 and 20 eV and a two-dimensional desorption pattern for $E=15$ eV. Arakawa, Takahashi, and Takeuchi[8] have studied the TOF distributions for metastable rare-gas atoms after impact of electrons with a constant energy of 200 eV. TOF distributions for metastable Ar atoms have also been obtained using the selective excitation possibilities of synchrotron radiation.[4,9]

In this paper, we extend the previously published work[7] and report a temporal sequence of desorption patterns for metastable Ar atoms. The desorption is induced by impact of 14.5-eV electrons on solid Ar(111). Combining the information on time-of-flight and angular distributions, several components in the metastable-atom signal can be resolved. Some aspects on the desorption mechanisms are given.

II. EXPERIMENT

The essential features of the spectrometer have been described in detail elsewhere.[7] Here we give only the basic elements and mention some recent improvements in the design. The system, shown in Fig. 1, is intended for low-energy electron diffraction (LEED) and angle-resolved electron-stimulated desorption (ESD) studies of condensed atoms and molecules including multilayer thin films. It is housed in a Mumetal, ultrahigh-vacuum chamber, which is ion- and cryo-pumped to a base pressure of 2×10^{-8} Pa. The electron beam, which exits a 127° cylindrical monochromator, has an energy resolution of 60 meV and reaches the target with an angular dispersion of 1° and a diameter of approximately 1 mm. The target holder is tilted by 18° with respect to the normal of the detection plane, which is identical to the electron-beam axis. The geometry of the arrangement allows for the collection of particles which emerge from the target within a cone subtended by an angle of 38°. The desorbed particles pass through a series of four spherically concentric LEED grids and two plane grids before reaching the detector. The grids allow discrimination of positively and/or negatively charged particles.

The detector consists of three large-area microchannel plates (MCP's) mounted in cascade in front of a resistive anode. The third MCP (standard 3-in. OD from Galileo) is a recent addition, which improves the sensitivity and uniformity of response across the detector beyond the performance demonstrated earlier.[7] This MCP is facing the target and thus determines the detection efficiency. From the detection of $N_2(A)$, the threshold internal energy for the detection of metastable particles is estimated to be around 7 eV. TOF measurements are performed by switching the electron beam on for a short period (≤ 10 μs) and subsequently recording only those particles which

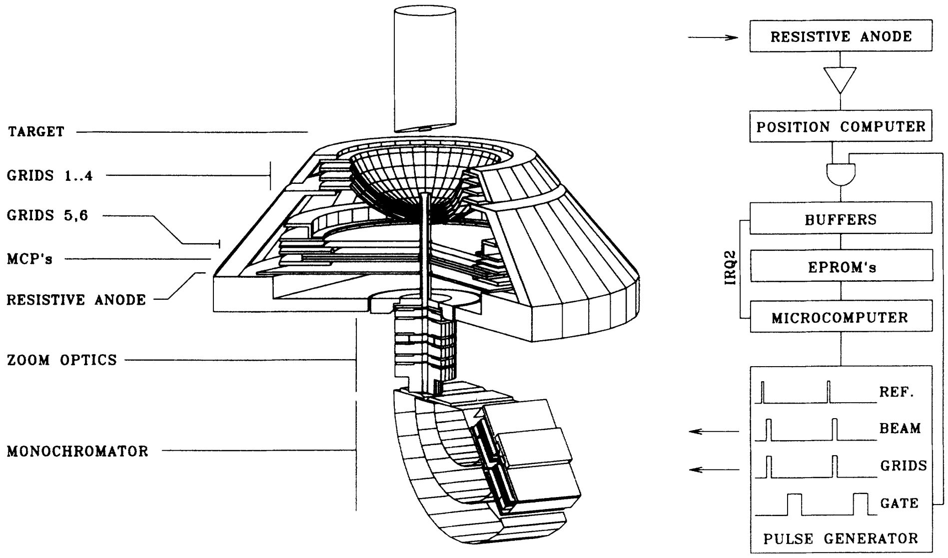

FIG. 1. Schematic view of the apparatus including the electron source, the LEED grids, the target, the detection system, the associated electronics, and the pulse sequence applied to the various components.

arrive at the detector during a second, delayed pulse. For the present series of experiments, the potentials at the grids $G1$-$G6$ (see Fig. 1) were set to repel all charged particles. The strong nonlinearities in the detector's spatial response are corrected by means of a hardware buffer which modifies the addresses of detected events as given by the position computer.[10]

Ar gas was supplied by Matheson of Canada Ltd. with a stated purity of 99.9995%. The films are grown onto a Pt(111) surface cleaned by argon-ion bombardment and annealed under oxygen flow. The target is mounted onto a closed-cycle helium cryostat, whose temperature can be varied between 300 and 14 K. The thickness of a film is determined from a calibration of the quantity of Ar required to form the monolayer, which is known from temperature-programmed desorption and low-energy electron transmission (LEET) measurements.[11] Films are deposited on the Pt surface at 24 K and then cooled to 18 K. This procedure permits the growth of a fcc Ar film with the (111) plane along the film-vacuum interface.[12] By measuring LEED patterns,[11] the Ar film has been found to consist in domains with a lattice parameter of 5.3±0.2 Å. Some of the domains are aligned with the Pt unit cell [Ar(111)*R*0°], while for the majority the unit cell is rotated by 30° [Ar(111)*R*30°]. By means of LEET, no charging of the film is observed over the course of an experiment. However, a decrease in the metastable-particle signal is discernible after approximately 60 min of electron bombardment, and therefore experimental runs are limited to periods of 30 min.

III. RESULTS

A. Time-resolved desorption patterns

In Fig. 2, a temporal sequence of desorption patterns from 100-layer Ar(111) films is given. The electron energy is 14.5 eV and thus 2.5 eV above the threshold for excitation of bulk excitons. The electron beam is striking the target for 5 μs every 300 μs, and the data collection is restricted to a time window 25 μs wide. The delay between the electron pulse and the acquisition window is increased in steps of 25 μs. The depicted patterns are obtained as the sum of the signals from several Ar films resulting in a total acquisition time of 30 min per pattern. Along with each frame, the delay between the rising edge of the electron pulse and the rising edge of the detection time window is indicated.

The first pattern (labeled 0 μs) is attributed to photons emitted during the decay of excited states within the bulk of the film, at the surface, or after ejection into the vacuum. The manifold of possible origins of the luminescence will be discussed in the next paragraph. We find the photon signal fairly isotropic within the detector plane and attribute the fluctuations to the detector's spatial response. The first pattern of Fig. 2 is therefore used for normalizing the signal in the subsequent time windows (labeled 25–175 μs). The signal in these time windows is due to metastable particles, since all the known fluorescent states have lifetimes much shorter than the present width of the detection time window.[13]

The intensity and the angular distribution of the desorbed metastable particles change with flight time. The intensity has decreased considerably at 25 μs in comparison with the photon signal, but it is still very broad. At 75 μs, a distinct feature appears indicating a narrow desorption cone. At 100 μs, the signal has increased its intensity across the entire detector and is now very bright in the region of the narrow cone. This cone is centered on the surface normal and has a width at half maximum of 8°. The signal indicates a fine beam of metastable atoms ejected normally from the surface with a kinetic energy of roughly 50 meV. The narrowness of this distribution is quite surprising considering the small kinetic

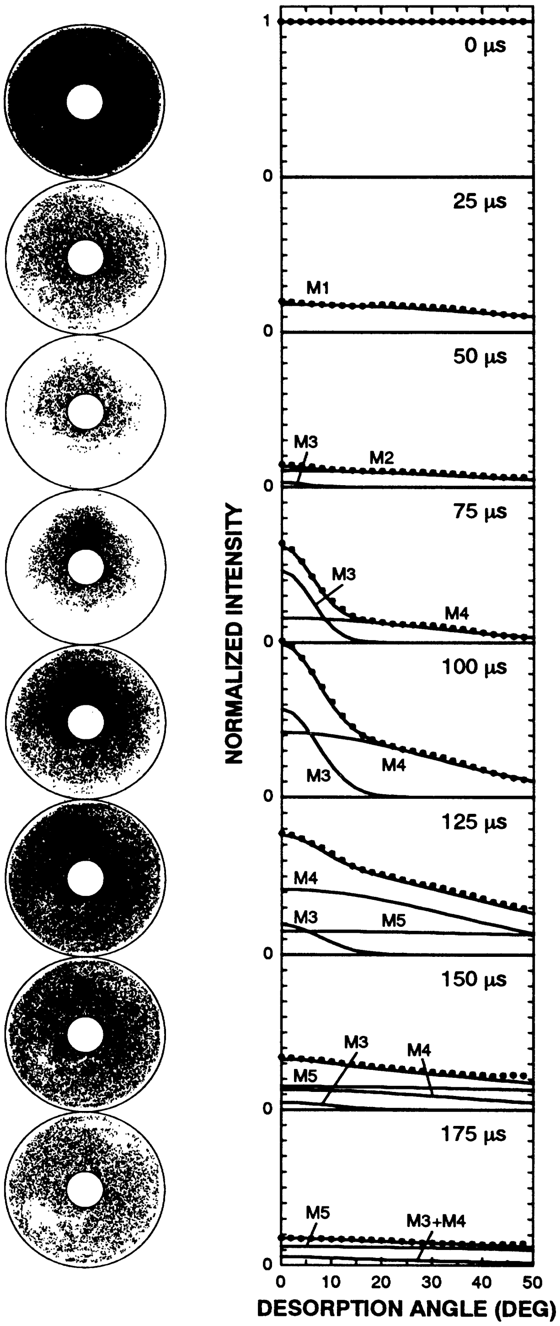

FIG. 2. Time-resolved Ar* desorption patterns from an Ar(111) film stimulated by 14.5-eV electrons. The electron pulse is on for 5 μs and the detection windows are 25 μs wide. The indicated time corresponds to the difference between the leading edges of the two pulses; the average time of flight for each pattern is 10 μs higher. On the right-hand side of each pattern, the normalized azimuthally integrated intensity distribution (dots) is given as a function of the polar angle θ together with the contributions of the different desorption components. See text for details.

energy of the ejected atoms, which makes them sensitive to surface imperfections and phonon scattering. At 125 μs, a bright diffuse signal dominates over the narrow distribution. As the time delay increases, the signal becomes more diffuse and the intensity decreases.

The main feature in the desorption patterns is the absence of azimuthal structure which makes it possible to increase the signal-to-noise ratio by summing the signal over concentric rings of 2° angular width around the point corresponding to normal ejection. The resulting angular distributions are displayed as a function of the polar angle θ next to each pattern in Fig. 2 (dots). The $\sin\theta$ term describing the different integration areas is already removed by normalizing on the photon signal. The detectable values of θ lie between 0° and 50° and we refer to each ring of 2° angular width by its low-angle value. Also included in these plots are the contributions from the different desorption components (solid lines $M1$-$M5$) as discussed in Sec. III B.

From the collected desorption patterns and angular distributions, low-resolution TOF spectra with a step size of 25 μs can be obtained. In Fig. 3, the TOF spectra for desorption angles between 0° and 50° are displayed. Changes in the TOF spectra with the angle of desorption suggest that several components with different angular distributions are superimposed in the total desorption yield.

B. High-resolution TOF spectrum

More information on the different velocity components is obtained from the high-resolution TOF spectrum (Fig. 4). The width of the detection time window is now 5 μs; the signal is integrated within a 20×20 pixel area (≈ 1 cm^2) on the detector plane centered at $\theta = 0°$. This region

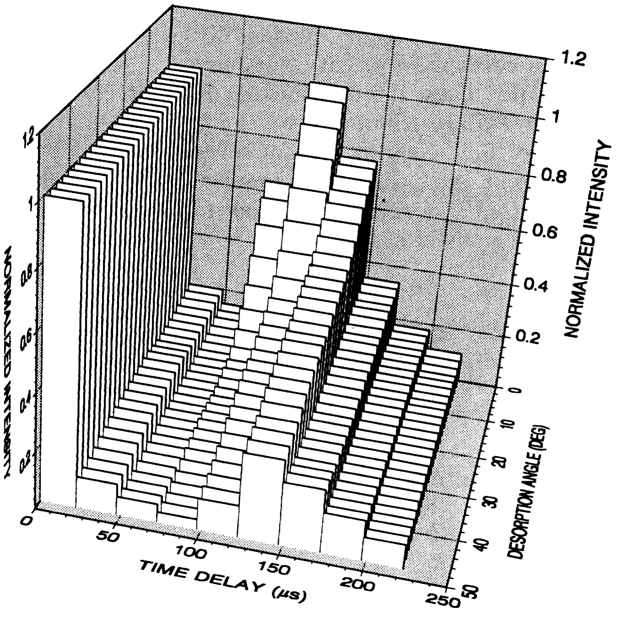

FIG. 3. Metastable Ar signal as function of time and desorption angle. For each angle, the signal is normalized to the photon signal (first time-window, 0–25 μs).

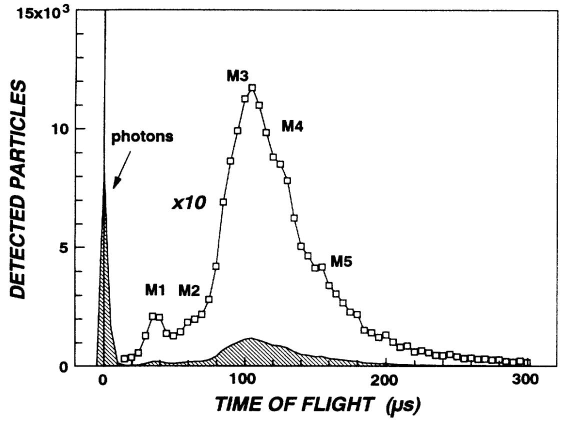

FIG. 4. High-resolution time-of-flight spectrum for the electron-stimulated desorption of metastable Ar atoms. The electron pulse and the detection window are both 5 μs wide. Possible structures in the metastable-particle signal are labeled.

contains signal from all components with some enhancement of the component with narrow angular distribution relative to the others. Clearly, the large signal at $t=0$ μs corresponds again to photon emission. With this time resolution, a realistic estimate for the fluorescent tail is possible.

Next, we assign structures in the high-resolution TOF spectrum in order to separate components with different physical origin in the metastable-particle signal. The spectrum shows a small structure at $t=40$ μs which is labeled $M1$. Next in time appears a stronger signal with a maximum at $t=100$ μs ($M3$) and shoulders at $t=75$ μs ($M2$) and $t=125$ μs ($M4$). From Figs. 2 and 3 it is apparent that these three structures display different angular behavior with $M3$ corresponding to the narrow-angle component. Additionally, we identify with less certainty a further component $M5$ at $t=160$ μs.

With this basic information on different components and their TOF distributions, we can fit the angular distributions of Fig. 2 as the sum of several components. In the present analysis, the angular distributions are parametrized in terms of Gaussian functions of variable amplitude and width.

$$I(\theta)=A\exp\left[-\frac{1}{2}\left[\frac{\theta}{\Delta\theta}\right]^2\right]. \tag{1}$$

The boundary conditions are automatically fulfilled by the normalization to the photon signal. It is straightforward to identify the $M3$ and $M4$ components in the angular distributions at $t=75$ and 100 μs. From the distributions at $t=50-125$ μs, fits for these two components are easily achieved, and similarly from the distributions at $t=150$ and 175 μs for $M5$. $M1$ is also determined unambiguously because it is the dominant component in the time window at 25 μs. From this starting point, we proceed to fit the weaker components for intermediate time windows. In some cases, several broad angular distributions overlap and the width for some components has to be taken from neighboring time windows, while the amplitude is still included in the fitting procedure. For the very broad $M5$ component only a lower limit for the angular width can be given. The resulting amplitudes and widths for the five angular distributions are given in Table I. We remark that the angular width of the $M3$ and of the $M4$ component is increasing with decreasing kinetic energy of the particles. These results will be discussed in the following section.

IV. DISCUSSION

A. General scheme

In a previous work,[7] the excitation functions of the photon signal and of particular velocity components of the metastable-particle signal have been correlated with high-resolution electron-energy-loss studies to show that the formation of free excitons (FE's) in the bulk of the film is the initial step in the deposition of electron energy. PSD studies corroborate this hypothesis and additionally show a clear contribution from surface FE's to the metastable-particle signal.[4,9]

To sketch the orders of magnitude of the involved processes, the dependence of the desorption yields on the thickness of the film has been analyzed[11] within a simple two-stream approximation.[14] The thickness dependence appears to be typical of an energy deposition within the bulk (as free exciton) followed by migration of the FE's

TABLE I. Amplitude A and width $\Delta\theta$ (deg) of the angular distributions [Eq. (1)] of the five desorption components in each relevant time window. Both values are given with respect to the photon signal. The angular distributions are displayed on the right-hand side of Fig. 2 (lines).

	$M1$		$M2$		$M3$		$M4$		$M5$	
t (μs)	A	$\Delta\theta$	A	$\Delta\theta$	A	$\Delta\theta$	A	$\Delta\theta$	A	$\Delta\theta$
25	0.181	46.6								
50			0.106	39.9	0.029	4.7				
75					0.461	5.7	0.157	28.4		
100					0.571	6.9	0.419	29.8		
125					0.191	7.4	0.417	33.5	0.150	>85
150					0.047	9.0	0.129	34.6	0.151	>85
175									0.121	>85
200									0.061	>85

within the film. This migration is accompanied by relaxation processes which ultimately lead to self-trapping within the film or at the film-vacuum interface, the former being the main source of luminescence and the latter leading to atomic self-trapping and desorption. The competition between free and self-trapped exciton states determines the mean free path of the FE which is of the order of 100 layer spacings. The interfaces (metal-film and film-vacuum) appear to be nearly perfect sinks for the free excitons.

Desorption therefore proceeds through either atomic or molecular self-trapping at the surface. In both cases, a cavity[15] is formed at the surface, which repels the excited particle and in favorable geometric environment may lead to desorption.[16] The coupling of the bulk FE to the self-trapped surface state can be either direct or via a surface FE. This general scheme is illustrated in Fig. 5, where the different states associated with the lowest excited atomic state are displayed for the three domains bulk, film surface, and vacuum.

A schematic survey of processes leading to photon emission is included in Fig. 5. Comparison with luminescence studies of condensed Ar indicates that the observed photon signal contains contributions from the radiative decay of several types of excited species: free-exciton states, trapped-exciton states, and excited atoms and dimers ejected into vacuum.[4] A contribution from inverse photoemission may also exist.[17] The high probability of self-trapping is revealed by the fact that the luminescence spectrum[4] is dominated by the decay of atomic (*a*-STE) and molecular (*m*-STE) self-trapped excitons, which are thought to resemble an excited Ar atom and an Ar excimer, respectively, embedded in the lattice.

The decay of the *a*-STE at the surface is identified with a luminescence peak at 11.55–11.58 eV.[18] Two broad bands of photons centered at 9.72 eV (*M* band) and at 11.38 eV (*W* band), respectively, are correlated with the *m*-STE.[4] The energy and width of the *M* band is very similar to the *M* band of Ar_2 in the gas phase (9.8 eV) which is attributed to decay from the Ar $^3\Sigma_u^+(0_u^+)$ and $^1\Sigma_u^+(1_u^+,0_u^-)$ excited states to the $^1\Sigma_g^+(0_g^+)$ ground state. Comparison with dense-gas luminescence has shown that the *M* band is due to the decay of vibrationally relaxed excimer states, the strong interaction with phonon modes in the solid being responsible for the relaxation. Similarly, the *W* band is associated with the decay from unrelaxed (vibrationally hot) $^3\Sigma_u^+(0_u^+)$ and $^1\Sigma_u^+(1_u^+,0_u^-)$ dimer states. It has recently been related to the decay of free excited dimers ejected into vacuum, where the relaxation time is much longer.[5]

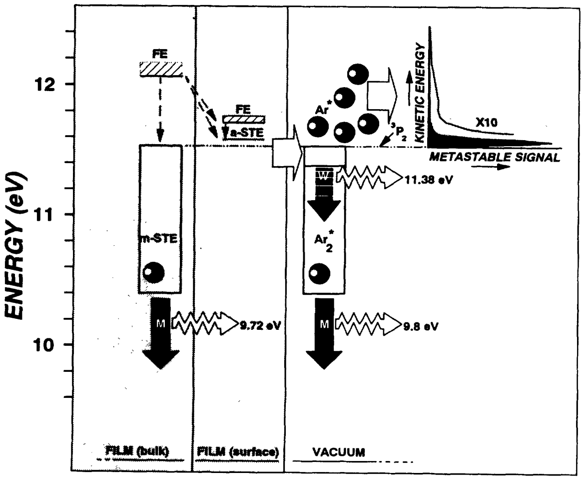

FIG. 5. Schematic survey of the various excited states of Ar in the bulk of a film, at the surface, and in the gas phase. The abbreviations and references are mentioned in the text. The observed dependence of the signal on the kinetic energy of the metastable particle (Fig. 6) is sketched in the inset.

The relatively long lifetime of the *m*-STE state (1.2 μs for the *M* band, Ref. 13) suggests that this state is responsible for the fluorescent tail of the photon signal in Fig. 4. In fact, the time dependence of the photon signal can be described approximately by assuming decay from the *m*-STE state exclusively, indicating that the contribution of transitions from the free-atom and *a*-STE states is small.

The delay times attributed to metastable particles ($t > 25$ μs) are much larger than any fluorescence lifetime previously seen in luminescence from Ar films.[13] It is therefore most likely that one or both of the lowest metastable Ar states ($[3p^5 4s]$ $^3P_2$ and $^3P_0$) are observed. Their lifetimes are 55.9 and 44.9 s, respectively.[19] We cannot completely discard the possibility of detecting excited dimers or clusters, but since the $^3\Sigma_u^+$ state, our prime candidate for a metastable dimer, has a lifetime of only 3.2 μs,[20] the detection of this excimer is quite unlikely. The luminescence after the decay of the excimer on the way to the detector will also be detected only in the first time window.

B. Kinetic-energy distributions

The kinetic energy (KE) of the desorbed atoms is calculated from the flight time assuming a unique mass $M = 40$ amu and target-MCP distance of $d = 52.5$ mm (along the normal of the film). The variation of this distance with the desorption angle is neglected since the effect on the KE determination is small compared to the effect of the width of the time windows. In principle, the signal must also be weighted by $\exp(t/\tau)$, where t is the flight time and τ the lifetime of the metastable atom. However, this correction is not necessary in the present case since the lifetimes of the detected species are much longer than their transit times in vacuum. The relation between the signal as a function of time of flight $P(t)$ and as a function of kinetic energy $P(E)$ then reads

$$E(t) = \frac{M}{2}\left[\frac{d}{t}\right]^2, \quad P(E(t)) = P(t)\left|\frac{dt}{dE}\right| = P(t)\frac{t^3}{Md^2} \tag{2}$$

with the well-known t^3 intensity modification. The kinetic-energy spectrum corresponding to the high-resolution TOF spectrum (Fig. 4) is depicted in Fig. 6. The influence of the t^3 term is obvious in the modified intensity ratio of fast and slow particles and in the structur-

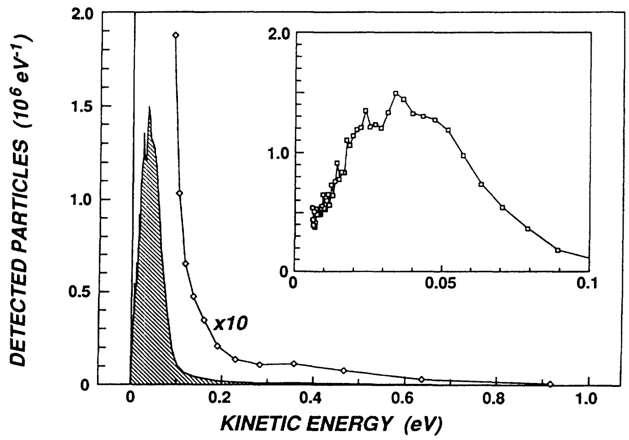

FIG. 6. Kinetic-energy spectrum of the desorbed metastable Ar atoms derived from Fig. 4 with Eq. (2). The low-energy part is given on an enlarged energy scale in the inset.

al changes within the main peak at around 105 μs (45 meV).

Due to the low time resolution in the two-dimensional (2D) TOF experiment, only the integrated distribution per time window $P_i(t_i)$ is known:

$$P_i(t_i)=\int_{t_i}^{t_i+\Delta t} P(t)dt \ . \tag{3}$$

In order to extract some information on $P(t)$ or $P(E)$ beyond the integrated values, we have to assume a certain functional dependence for the time of flight or kinetic-energy distribution of the observed components. The straightforward trial function is a Gaussian KE distribution with variable amplitude and width. This selection is supported by the general shape of the $M3$, $M4$, and $M5$ components in the low-resolution TOF spectrum (Fig. 3, Table I). It can be rationalized by a simple Franck-Condon-like picture based on the instantaneous response of the electron cloud to a given nuclear configuration. The final KE distribution is then given as the reflection of the ground-state intensity at the excited-state potential. We assume a harmonic potential for the electronic ground state and a repulsive potential-energy surface for the excited atom-surface complex, which is to a first approximation linear along the direction of desorption. With the surface being initially in the vibrational ground state, the final KE distribution has a Gaussian shape. Its width is modified by the steepness of the excited-state potential and its energy at the maximum is given as the difference between the potential at the equilibrium point and the large-distance potential. The resulting function used to fit the time-of-flight distributions is

$$P(t)=B\frac{Md^2}{t^3}\exp\left[-\frac{1}{2}\left[\frac{Md^2/2t^2-E_0}{\Delta E}\right]^2\right] . \tag{4}$$

In a first step, we have attempted to fit the TOF signal $P_i(t_i)$ of the components $M3$, $M4$, and $M5$. It is, however, not possible to describe $M4$ correctly with (3) and (4). A possible reason could be the extension of the $M2$ component to flight times higher than assumed before resulting in a $M2$ contribution to the signal at $t=75$ μs, which was originally ascribed to $M4$. Consequently, only the points at 100, 125, and 150 μs are considered to represent the undisturbed TOF distribution of the $M4$ component. Alternatively, it could be possible that this component consists of two groups which cannot be resolved in the present approach. The KE distributions for the $M1$ and $M2$ components cannot be extracted from the low-resolution TOF spectrum because a large part, if not all, of the signal is detected within a single time window. The high-resolution TOF spectrum (Fig. 4), however, provides enough information to allow the determination of the width of the KE distributions. Their amplitudes can then be obtained from the 2D TOF data.

The metastable-atoms distributions are found to peak at kinetic energies of about 19 ($M5$), 36 ($M4$), 53 ($M3$), 85 ($M2$), and 345 meV ($M1$) with ΔE values of 11 ($M5$), 11 ($M4$), 19 ($M3$), 53 ($M2$), and 191 meV ($M1$), respectively. We estimate the uncertainty of the numerical values to be of the order of 10%. These results are compiled in Table II, where the amplitude B of the distributions is given as the number of metastable atoms (normalized to the number of emitted photons) per eV of KE. The TOF distributions of the individual components as obtained by this procedure are depicted in Fig. 7.

The relative populations of the components can now be obtained by integrating the angular and kinetic-energy distributions. Setting the photon yield to 1, the total desorption intensities are 0.41–0.72 ($M5$, 85° width or isotropic), 0.25 ($M4$), 0.08 ($M1$), 0.08 ($M2$), and 0.08 ($M3$). The total metastable-particle signal is 0.9–1.2 times the total photon signal assuming that the sensitivity of the MCP's is the same for both types of particles. These results are also included in Table II. They again underline the high probability of exciton self-trapping at the surface since the metastable-particle signal is exclusively based on surface excitation, whereas the photon signal has major contributions from the bulk of the film.

The present results for the kinetic-energy distributions may be compared with similar results of Arakawa, Takahashi, and Takeuchi.[8] Using an electron beam with $E=200$ eV, these authors obtained a TOF spectrum for excited Ar atoms from a 1000-ML Ar film. Two peaks appear in the spectrum and the corresponding energy values are given as 0.04 eV [full width at half maximum

TABLE II. Amplitude B, central value E_0, and width ΔE of the Gaussian kinetic-energy distributions of the five desorption components. Also given is the total yield for each component (integrated over kinetic energy and desorption angle). The two values for the integral yield of the $M5$ component correspond to either $\Delta\theta=85°$ or isotropic angular distribution.

	$M1$	$M2$	$M3$	$M4$	$M5$	
B (eV^{-1})	0.52	2.0	28	38	25	
ΔE (eV)	0.191	0.053	0.019	0.011	0.011	
E_0 (eV)	0.345	0.085	0.053	0.036	0.019	
						total
integral	0.08	0.08	0.08	0.25	0.41	0.89
					0.72	1.20

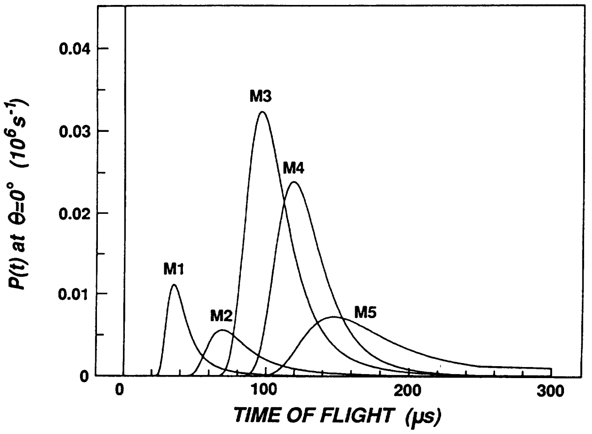

FIG. 7. Time-of-flight distributions $P(t)$ of the five identified desorption components [see Eq. (3)]. The relative intensities depend on the polar angle and the $M3$ component is especially pronounced at $\theta=0°$.

(FWHM) 0.04 eV] and 0.6 eV (FWHM 0.4 eV). The similarity with the present results is obvious. The low-energy signal is identified with the unresolved sum of the $M2$-$M5$ components (compare Fig. 6), while the high-energy signal should correspond to $M1$. The difference in energy may be accounted for partly by the fact that the value of Arakawa, Takahashi, and Takeuchi refers to the maximum of $P(t)$ and according to (2) a considerable shift has to be expected for the maximum of $P(E)$. Moreover, the effect of timing uncertainties on the energy determination is more pronounced for the higher energies.

Arakawa and Sakurai performed a further experiment with photon excitation[9] and found essentially the same two peak positions. The high-energy signal is weak for a photon energy of 13.8 eV and absent for 12.2 eV, indicating the excitation of a higher-excited exciton as precursor to this signal. For a photon energy of 11.8 eV corresponding to the excitation of the lowest surface exciton, Kloiber and Zimmerer[6] found in a time-of-flight experiment an energy distribution with a peak at 0.042 eV and a width of 0.045 eV (FWHM). A further structure at 0.42 eV is only weakly indicated. The similarity of the results obtained using high-energy electrons, low-energy electrons, or photons implies that the desorption kinetics is governed by the intermediate electronic excitation in the film. Only the branching ratio between the slow and the fast components depends on the first step in the desorption process, where the energy is transferred from the impinging particle to the electronic excitation in the film (excitons, free-electron–hole pairs).

The different desorption components are attributed to the dynamics of atomic and molecular self-trapped excitons. The fast metastable atom is possibly related to the decay of a higher-excited m-STE

$$\mathrm{Ar}_2^{**} \rightarrow \mathrm{Ar}^* + \mathrm{Ar} + E_{\mathrm{kin}} \tag{5}$$

similar to the process leading to the fast ground-state component.[2] Since the excitation level of process (5) is higher, the intensity of fast metastable atoms is much lower than the intensity of fast ground-state atoms. To our knowledge, no calculations on the energy distribution for fast Ar* have been published.

The basic feature of the a-STE is the cavity around the excited atom due to electron repulsion. If the a-STE is located at the surface, the forces on the excited atom do not compensate and the net force is directed into the vacuum.[15] Molecular-dynamics studies of Cui, Johnson, and Cummings[16] show that the kinetic energy crucially depends on the number of neighboring atoms. Although the numerical results differ for the different model interaction potentials used, the kinetic energies always lie in the range between 0 and 100 meV and vary with the number of neighbors by roughly 15–20 meV per atom. The highest kinetic energy is obtained for a complete environment with six nearest neighbors in the surface plane. The high symmetry of this geometry is broken if one or more atoms are missing and therefore the angular distribution, now a sum of several non-normal components, is broadened. In this context, the $M3$ component with a kinetic energy centered at 53 meV and a narrow angular distribution is identified with the desorption from a locally perfect environment at the film surface. The $M4$ and $M5$ components correspond then to sites with five and four nearest neighbors, respectively. Their kinetic energies are smaller by 17 meV per missing neighbor and their angular distributions are gradually broadening with respect to the $M3$ values. An extrapolation to the next component in this series gives a kinetic energy close to zero leaving the respective particles outside of the detection range of the present TOF experiments.

The $M2$ component does not fit into the mentioned scheme of constantly increasing kinetic energy and decreasing angular width. Its kinetic-energy distribution is also relatively broad. At present, we cannot decide if the precursor is an atomic or a molecular STE. Possible mechanisms are the desorption from a decaying higher-excited a-STE or energy (and excitation) transfer processes of a fast Ar* which is not directly leaving the film after the decay of the m-STE.

C. Angular distributions

After using the angular dependence of the metastable-particle signal simply as a means to identify several desorption components, we focus in this section on some aspects of the physical origin of the observed distributions. Generally, angle-resolved ESD gives a picture of the short-range interaction between a desorbing atom and the substrate (see Ref. 21 for a recent review). The angular distribution often reflects a well-defined crystalline structure of the substrate, especially in the case of a pronounced dependence on the azimuthal angle. If, however, a particular angular distribution is azimuthally invariant, it is not obvious whether to ascribe this behavior to an azimuthally invariant short-range interaction or to the averaging effect of either long-range interaction or surface disorder. As mentioned before, two domains with different orientation have been found for the present Ar films, and at their boundaries no well-defined crystalline structure exists. Within a domain, variable structure is also expected due to a partly filled top layer and dislocations. These defects should have the tendency to wash off angular structures observable in a perfect crystal. Additionally, relaxation processes during desorption can destroy the angular information.

The $M3$ component appears to be a suitable candidate for studying the intrinsic features of an undistorted angular distribution. It is thought to reflect desorption from a fully symmetric part of the surface where the net force on the desorbed particle is centered around the surface normal. The angular width of this component increases slightly with the kinetic energy of the desorbed atom as described before (Table I). This dependence is depicted in Fig. 8 where the momentum parallel to the surface $p_{\parallel}$ (calculated from the width at half maximum of the angular distribution at a particular energy) is given as a function of the total momentum p.

Assuming again a Franck-Condon-like excitation, the momentum distribution Δp in the ground state will be preserved during the transition and contribute to $p_{\parallel}$. The zero-point momentum for a particle with mass M in a harmonic potential

$$V(r)=\tfrac{1}{2}Cr^2 \tag{6}$$

is on the order of

$$\Delta p \approx \tfrac{1}{2}(CM\hbar^2)^{1/4} \; . \tag{7}$$

The force constant acting on a ground-state atom at equilibrium position in the surface plane is calculated from the dimer potential of Aziz and Chen[22] to $C(\theta=\pi,\phi)\approx 1.9$ eV Å^{-2}, leading to a value for Δp of $6\hbar$ Å^{-1}. This is just the order of magnitude observed in our experiment for the $M3$ component. Gortel and Wierzbicki[23] pointed out that the zero-point energy gained in the intermediate excited state might be crucial for the desorption of neutral ground-state Ar or N_2O from Ru (001) and they achieve good agreement with experimental results on the kinetic-energy distribution. In the present case, where the excited state is directly expelling the atom, its influence on the zero-point momentum is given by the time-dependent evolution of the system. In a simple picture, it might be assumed that the curvature of the excited-state potential is decreasing with increasing atom-surface distance z. Regarding the fact that the potential energy of the excited state has a similar general trend, the observed relation between the parallel momentum $p_{\parallel}$ and the total momentum p may be rationalized. A transition at a point $z > z_0$ corresponds then to a lower kinetic energy and a lower angular spread of the desorbed atoms than a transition at $z < z_0$.

Another contribution to $p_{\parallel}$ is based on the interaction of the excitation with phonon modes. The maximum momentum of a phonon in an Ar lattice with a nearest-neighbor distance $a=3.75$ Å (Ref. 13) is $p_{\max}\approx\hbar\pi/a=0.84\hbar$ Å^{-1}. It is perhaps reasonable to expect the energy loss to phonons being proportional to the total excitation energy. Multiphonon excitation must therefore be regarded in a quantitative discussion of both, the observed value of the momentum parallel to the surface and its increase with the total momentum.

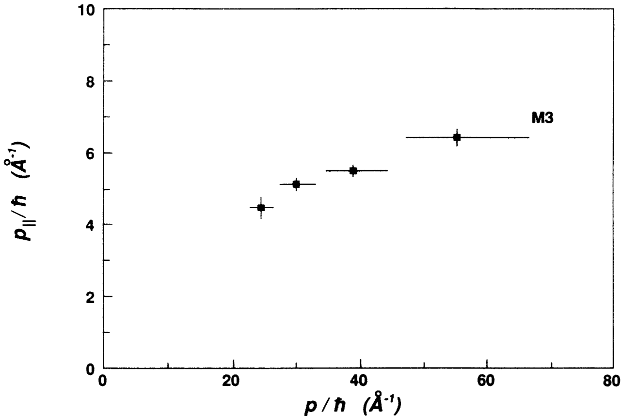

FIG. 8. Dependence of the average momentum parallel to the surface plane $p_{\parallel}$ on the total momentum p for the $M3$ component. The given $p_{\parallel}$ corresponds to the angle at half maximum of the angular distribution for a particular time window, p is calculated from the central time of flight in this time window.

V. CONCLUSIONS

The use of time- and angle-resolved detection in ESD provides a wealth of information by allowing one to discriminate between distinct components of metastable atoms desorbed from a crystalline Ar film. From the present experimental results it is possible for us to resolve five metastable-atom components with different kinetic-energy and angular distributions. They can be identified within the general framework of the exciton-relaxation scheme. One component with a kinetic energy centered at 53 meV and a narrow angular distribution in the order of magnitude introduced by the nuclear zero-point motion is ascribed to the desorption from an a-STE in a defectless local environment. The two lower-energy components with a kinetic energy centered at 36 and 19 meV correspond, according to molecular-dynamics studies, to Ar* emission from Ar(111) surface sites missing one or two nearest neighbors, respectively. Within this description, the higher-KE components can be ascribed to desorption from higher-energy decaying a-STE or m-STE states. For a more quantitative understanding of the observed features, it would be highly desirable to perform molecular-dynamics studies with reliable potentials of the interaction between the excited atom and the crystal. We hope that the present results will have some impact on the further development of this avenue.

ACKNOWLEDGMENTS

We thank Paul A. Rowntree for his constant interest in the progress of this work and useful discussions. The work was sponsored by the Medical Research Council of Canada.

[1] E. Hudel, E. Steinacker, and P. Feulner, Phys. Rev. B **44**, 8972 (1991).

[2] C. T. Reimann, W. L. Brown, and R. E. Johnson, Phys. Rev. B **37**, 1455 (1988).

[3] C. Feulner, T. Müller, A. Puschmann, and D. Menzel, Phys. Rev. Lett. **59**, 791 (1987).

[4] T. Kloiber and G. Zimmerer, Radiat. Eff. Def. Solids **109**, 219 (1989).

[5] C. T. Reimann, W. L. Brown, M. J. Nowakowski, S. T. Cui, and R. E. Johnson, in *Desorption Induced by Electronic Transitions DIET IV*, edited by G. Betz and P. Varga (Springer-Verlag, Berlin, 1990), p. 226.

[6] T. Kloiber and G. Zimmerer, Phys. Scr. **41**, 962 (1990).

[7] G. Leclerc, A. D. Bass, M. Michaud, and L. Sanche, J. Electron Spectrosc. Relat. Phenom. **52**, 725 (1990).

[8] I. Arakawa, M. Takahashi, and K. Takeuchi, J. Vac. Sci. Technol. A **7**, 2090 (1989).

[9] I. Arakawa and M. Sakurai, in *Desorption Induced by Electronic Transitions DIET IV* (Ref. 5), p. 246.

[10] G. Leclerc, J.-B. Ozenne, J.-P. Corbeil, and L. Sanche, Rev. Sci. Instrum. **62**, 2997 (1991).

[11] G. Leclerc, Ph.D. thesis, Université de Sherbrooke, 1991.

[12] M. Michaud, L. Sanche, C. Gaubert, and R. Baudoing, Surf. Sci. **205**, 447 (1988); M. Michaud, P. Cloutier, and L. Sanche, Phys. Rev. B **44**, 10 485 (1991).

[13] G. Zimmerer, in *Excited-State Spectroscopy in Solids,* edited by U. Grassano and N. Terzi (North-Holland, Amsterdam, 1987), p. 37.

[14] P. J. Chantry, A. V. Phelps, and G. J. Schulz, Phys. Rev. **152**, 81 (1966).

[15] F. Coletti, J. M. Debever, and G. Zimmerer, J. Phys. (Paris) Lett. **45**, L467 (1984).

[16] S. T. Cui, R. E. Johnson, and P. T. Cummings, Phys. Rev. B **39**, 9580 (1989).

[17] K. Horn, K. H. Frank, J. A. Wilder, and B. Reihl, Phys. Rev. Lett. **57**, 1064 (1986).

[18] M. Joppien, F. Grotelüschen, T. Kloiber, M. Lengen, T. Möller, J. Wörmer, G. Zimmerer, J. Keto, M. Kytka, and M. C. Castex, J. Lumin. **48&49**, 601 (1991).

[19] N. E. Small-Warren and L.-Y. Chow Chiu, Phys. Rev. A **11**, 1777 (1975).

[20] J. W. Keto, R. E. Gleason, Jr., and G. K. Walters, Phys. Rev. Lett. **23**, 1365 (1974).

[21] R. D. Ramsier and J. T. Yates, Jr., Surf. Sci. Rep. **12**, 246 (1991).

[22] R. A. Aziz and H. H. Chen, J. Chem. Phys. **67**, 5719 (1977).

[23] Z. W. Gortel and A. Wierzbicki, Surf. Sci. Lett. **239**, L565 (1990).

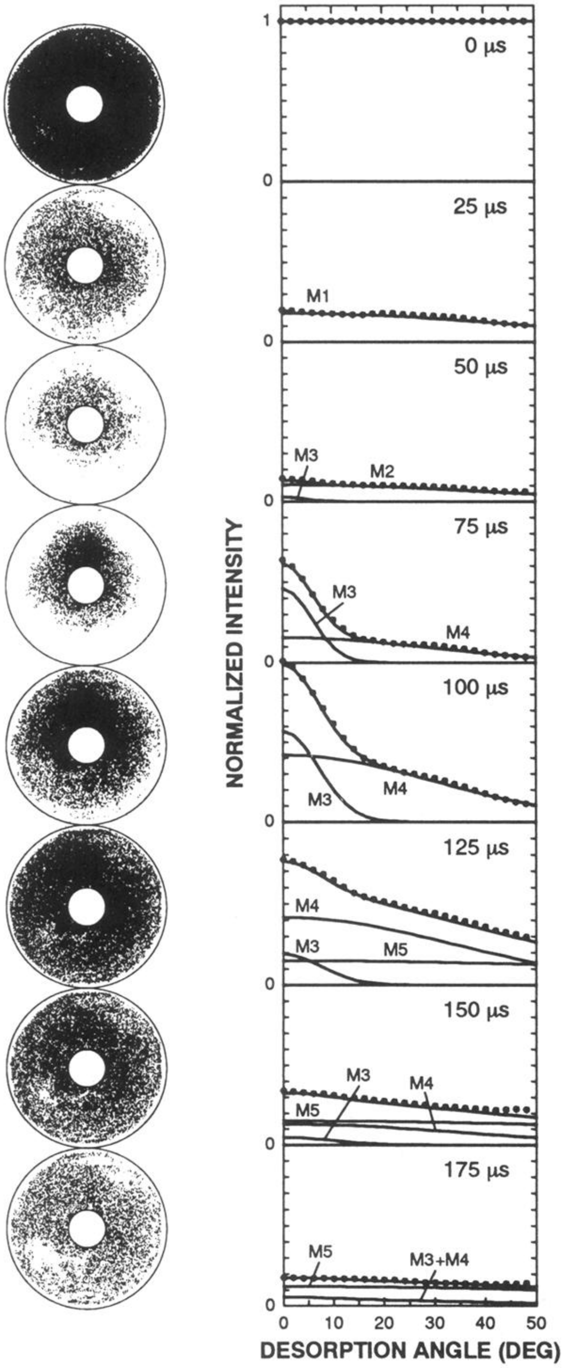

FIG. 2. Time-resolved Ar* desorption patterns from an Ar(111) film stimulated by 14.5-eV electrons. The electron pulse is on for 5 μs and the detection windows are 25 μs wide. The indicated time corresponds to the difference between the leading edges of the two pulses; the average time of flight for each pattern is 10 μs higher. On the right-hand side of each pattern, the normalized azimuthally integrated intensity distribution (dots) is given as a function of the polar angle θ together with the contributions of the different desorption components. See text for details.

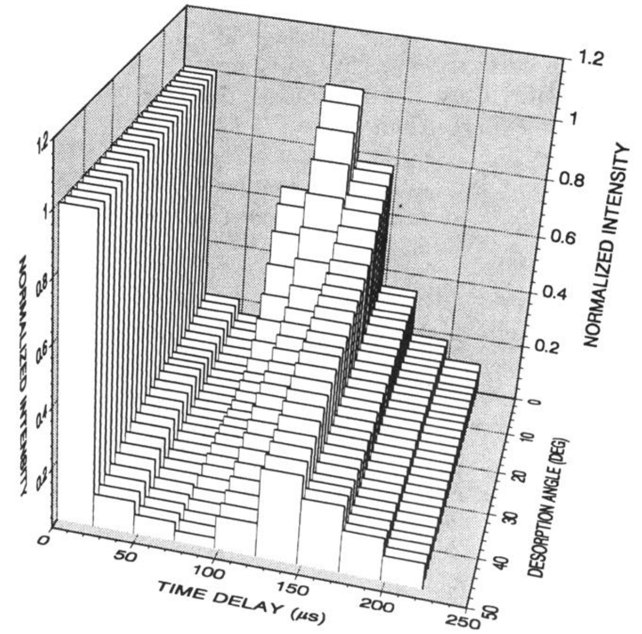

FIG. 3. Metastable Ar signal as function of time and desorption angle. For each angle, the signal is normalized to the photon signal (first time-window, 0–25 μs).

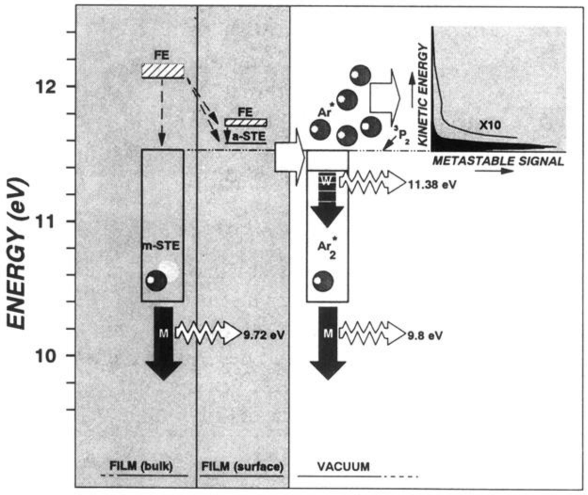

FIG. 5. Schematic survey of the various excited states of Ar in the bulk of a film, at the surface, and in the gas phase. The abbreviations and references are mentioned in the text. The observed dependence of the signal on the kinetic energy of the metastable particle (Fig. 6) is sketched in the inset.